arXiv:1609.07114v1 [cs.CE] 22 Sep 2016

A Stable FDTD Method with Embedded Reduced-Order Models

Xinyue Zhang, Fadime Bekmambetova, and Piero Triverio, *Senior Member, IEEE*

***Abstract*—The computational efficiency of the Finite-Difference Time-Domain (FDTD) method can be significantly reduced by the presence of complex objects with fine features. Small geometrical details impose a fine mesh and a reduced time step, significantly increasing computational cost. Model order reduction has been proposed as a systematic way to generate compact models for complex objects, that one can then instantiate into a main FDTD mesh. However, the stability of FDTD with embedded reduced models remains an open problem. We propose a systematic method to generate reduced models for FDTD domains, and embed them into a main FDTD mesh with *guaranteed stability*. Models can be created for arbitrary domains containing inhomogeneous and lossy materials. The Courant-Friedrichs-Lewy (CFL) limit of the final scheme is provided by the theory, and can be extended with a simple perturbation of the coefficients of the reduced models. Numerical tests confirm the stability of the proposed method, and its potential to accelerate multiscale FDTD simulations.**

***Index Terms*—Finite-Difference Time-Domain method, model order reduction, subgridding, CFL limit extension, stability, passivity.**

I. Introduction

The Finite-Difference Time-Domain (FDTD) method solves Maxwell's equations numerically using a staggered grid, where the electric and magnetic fields are sampled at alternate nodes [1], [2]. This configuration is particularly convenient to discretize the curl operators in Maxwell's equations. An attractive feature of FDTD is the use of an explicit leap-frog scheme to march in time. This approach significantly reduces the cost per iteration over implicit alternatives, but makes stability conditional to the well-known Courant-Friedrichs-Lewy (CFL) condition [2]. In 2D, the CFL condition reads

$$\Delta t < \frac{1}{c\sqrt{\frac{1}{\Delta x^2}+\frac{1}{\Delta y^2}}}, \tag{1}$$

where Δt is time step, Δx and Δy are the cell dimensions along the x and y axes, and c is the wave velocity in the medium [2].

Unfortunately, in spite of its low cost per iteration, FDTD can become quite time-consuming when applied to large multiscale problems with detailed objects. Two issues contribute to the increase of FDTD's cost:

Manuscript received ...; revised ...

This work was supported in part by the Natural Sciences and Engineering Research Council of Canada (Discovery grant program) and in part by the Canada Research Chairs program.

X. Zhang, F. Bekmambetova, and P. Triverio are with the Edward S. Rogers Sr. Department of Electrical and Computer Engineering, University of Toronto, Toronto, M5S 3G4 Canada (email: xinyuezhang.zhang@mail.utoronto.ca, fadime.bekmambetova@mail.utoronto.ca, piero.triverio@utoronto.ca).

a) small details impose a refined mesh. This increases memory consumption and cost per iteration;
b) a refined mesh implies a shorter time step because of CFL limit (1).

Numerous solutions have been devised to increase FDTD's efficiency in handling complex objects. Subcell models have been proposed for wires [3], wire bundles [4], sheets [5], slots [6], and other common structures. In FDTD subgridding, a fine mesh is used to resolve small objects, while a coarse grid is used elsewhere [7], [8]. These models are typically efficient, but restricted to specific objects. Subgridding reduces the growth of the number of unknowns caused by mesh refinement (issue a in the list above). However, it does not help with the second issue, since the fine grid imposes its CFL limit on the whole domain. While different time steps can be used in the coarse and fine grids, ensuring the stability and accuracy of the resulting scheme is quite challenging [9].

Model order reduction (MOR) has been proposed to generate compact FDTD models for complex objects [10], [11], [12]. The underlying idea is to initially use a fine mesh to resolve complex objects, and then compress the FDTD equations using MOR. The reduced model is finally embedded into the surrounding coarse grid [11]. Typically, the insertion of the reduced model in the coarse grid reduces the CFL limit. However, because of its low order, the reduced model can be manipulated to extend the CFL limit, and enable the use of a larger time step throughout the entire computational domain [13], [14], [15]. Therefore, an MOR-based approach can be used to tackle both issues a) and b) caused by mesh refinement.

While MOR has clearly the potential to accelerate multiscale FDTD simulations, its use has been so far limited by stability considerations. When a reduced model is embedded into a main FDTD grid, it can easily lead to instability. Unfortunately, this happens even if the reduced model, by itself, is stable [11]. Kulas and Mrozowski [16] investigated the stability of an FDTD scheme with macromodels, and derived a reciprocity condition for stability. An expression for the CFL limit of the resulting scheme is also provided. There are two main limitations in this work. First, the derivation is valid only for the lossless case. Second, the expression for the CFL limit requires the norm of a very large matrix. For realistic problems, such norm cannot be computed. An upper bounds can be derived, but it leads to a conservative CFL limit. Moreover, the estimation becomes more involved when multiple reduced models are embedded into the main grid.

In this paper, we propose a systematic theory to generate reduced models for FDTD regions, and couple them to a main

FDTD grid with guaranteed stability. The method provides a strict CFL limit of the final scheme, and is valid in the general case of lossy inhomogeneous materials. The regions with complex objects are first meshed with a refined grid. The FDTD equations for those regions are written in the form of a discrete-time dynamical system with inputs and outputs, as described in Sec. II. The system is reduced with a MOR method that preserves the structure of FDTD equations (see Sec. III). A stable method to couple the reduced model to the main coarse grid is proposed in Sec. IV. In Sec. V, we prove that the obtained scheme is stable by construction up to the CFL limit of the finest grid. The proof is based on a novel stability theory for FDTD based on dissipative systems [17]. Finally, we show that, with a simple perturbation of the reduced model coefficients, the CFL limit of the final scheme can be controlled and extended. There are several novel aspects in this work. First, the proposed theory is general, since it accounts for losses that were previously neglected [16]. Second, the stability of the final scheme is controlled by simple conditions imposed independently on each reduced model. This feature is a significant advantage over previous works [16], whose stability conditions involve the whole domain (coarse grid plus all reduced models). As a result, the proposed theory is straightforward to apply even when numerous models are embedded into a main FDTD grid. Third, the novel stability conditions provide a stringent CFL limit for the whole scheme. The numerical examples in Sec. VI confirm the stability of the proposed methodology, and its ability to accelerate multiscale FDTD simulations.

II. FDTD Equations for the Fine Grid as a Discrete-Time Dynamical System

We consider a multiscale scenario where several objects with fine features are present in a large two-dimensional domain. As in subgridding, we use a fine mesh in the regions with fine features. A coarse mesh is used in the rest of the domain. Without loss of generality, we consider the case of a single region with fine mesh. The extension to multiple regions is straightforward since the same process can be independently applied to each refined region. The cell dimensions in the coarse grid are denoted as Δx and Δy. In the fine region, the cell dimensions are

$$\Delta\hat{x} = \frac{\Delta x}{r}\,, \qquad \Delta\hat{y} = \frac{\Delta y}{r}\,, \tag{2}$$

where the refinement factor $r > 1$ is an integer. Throughout the paper, we use symbols with a hat for the quantities associated with the fine grid, and symbols with no hat for the quantities associated with the coarse grid. In order to later apply MOR, we cast the FDTD equations for the fine region in the form of a discrete-time dynamical system, having the E and H field tangential to the region boundaries as inputs and outputs [17]. These variables will allow us to reconnect the reduced model of the fine grid to the main grid.

A. FDTD Update Equations for the Nodes of the Fine Mesh

We consider a rectangular fine mesh with $\hat{N}_x$ cells along x and $\hat{N}_y$ cells along y. A graphical illustration of a simple 2×2 region is provided in Fig. 1. We consider a TE$_z$ mode with field components E_x, E_y and H_z. In addition to the standard field samples used in FDTD, we also take as variable the magnetic field on the four boundaries of the region, as shown in Fig. 1. These samples are called hanging variables [18], and serve two purposes. First, they allow us to write a self-contained mathematical model for the region, which does not involve any field sample beyond its boundaries [17]. Second, hanging variables will facilitate the connection of the fine region model to the surrounding coarse grid.

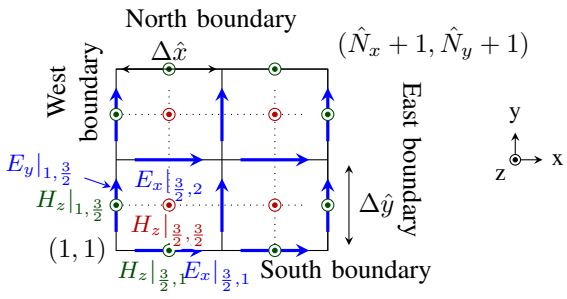

Fig. 1. Graphical illustration of a simple 2×2 fine region. The solid lines denote the primary grid. The green color denotes the hanging variables introduced on the four boundaries.

1) Update Equations for the E_x and E_y Nodes: For the E_x nodes that are strictly inside the fine region, we write a standard FDTD update equation [2]

$$\Delta\hat{x}\Delta\hat{y}\left(\frac{\varepsilon_x}{\Delta t}+\frac{\sigma_x}{2}\right)E_x|^{n+1}_{i+\frac{1}{2},j} = \Delta\hat{x}\Delta\hat{y}\left(\frac{\varepsilon_x}{\Delta t}-\frac{\sigma_x}{2}\right)E_x|^{n}_{i+\frac{1}{2},j} + \Delta\hat{x}H_z|^{n+\frac{1}{2}}_{i+\frac{1}{2},j+\frac{1}{2}} - \Delta\hat{x}H_z|^{n+\frac{1}{2}}_{i+\frac{1}{2},j-\frac{1}{2}}\,, \tag{3}$$

where ε_x and σ_x are, respectively, the average permittivity and conductivity on the x-oriented edges of the primary grid[1]. For the nodes on the South and North boundaries of the region, a modified FDTD equation must be used [17]. A conventional FDTD equation would otherwise involve magnetic fields beyond the region boundaries, that may not even be available because of the different resolution used in the surrounding coarse grid. This issue can be avoided by using the hanging variables to approximate the spatial derivatives of the magnetic field on the boundaries. For instance, the following update equation is written for the E_x nodes on the South boundary [17]

$$\Delta\hat{x}\frac{\Delta\hat{y}}{2}\left(\frac{\varepsilon_x}{\Delta t}+\frac{\sigma_x}{2}\right)E_x|^{n+1}_{i+\frac{1}{2},1} = \Delta\hat{x}\frac{\Delta\hat{y}}{2}\left(\frac{\varepsilon_x}{\Delta t}-\frac{\sigma_x}{2}\right)E_x|^{n}_{i+\frac{1}{2},1} + \Delta\hat{x}H_z|^{n+\frac{1}{2}}_{i+\frac{1}{2},1+\frac{1}{2}} - \Delta\hat{x}H_z|^{n+\frac{1}{2}}_{i+\frac{1}{2},1}\,. \tag{4}$$

A similar equation can be derived to update the E_x nodes on the North boundary. The same approach is followed to write the update equations for the E_y nodes. A conventional FDTD equation is used for the E_y nodes that fall strictly inside the region, while a modified equation involving hanging variables

[1]To keep expressions reasonably compact, we do not indicate explicitly the dependence of ε_x, σ_x, ε_y, σ_y and μ from i and j.

is used for the nodes on the West and East boundaries [17]. All together, the update equations for all E_x and E_y samples can be written in a compact matrix form [17]

$$\hat{\mathbf{D}}_{l_x}\hat{\mathbf{D}}_{l'_y}\left(\frac{\hat{\mathbf{D}}_{\varepsilon_x}}{\Delta t}+\frac{\hat{\mathbf{D}}_{\sigma_x}}{2}\right)\hat{\mathbf{E}}_x^{n+1} = \hat{\mathbf{D}}_{l_x}\hat{\mathbf{D}}_{l'_y}\left(\frac{\hat{\mathbf{D}}_{\varepsilon_x}}{\Delta t}-\frac{\hat{\mathbf{D}}_{\sigma_x}}{2}\right)\hat{\mathbf{E}}_x^{n} - \hat{\mathbf{D}}_{l_x}\hat{\mathbf{G}}_y^T\hat{\mathbf{H}}_z^{n+\frac{1}{2}} + \begin{bmatrix}\hat{\mathbf{D}}_{l_x}\hat{\mathbf{B}}_S & \hat{\mathbf{D}}_{l_x}\hat{\mathbf{B}}_N\end{bmatrix}\begin{bmatrix}\hat{\mathbf{H}}_S^{n+\frac{1}{2}}\\ \hat{\mathbf{H}}_N^{n+\frac{1}{2}}\end{bmatrix}, \quad (5)$$

$$\hat{\mathbf{D}}_{l_y}\hat{\mathbf{D}}_{l'_x}\left(\frac{\hat{\mathbf{D}}_{\varepsilon_y}}{\Delta t}+\frac{\hat{\mathbf{D}}_{\sigma_y}}{2}\right)\hat{\mathbf{E}}_y^{n+1} = \hat{\mathbf{D}}_{l_y}\hat{\mathbf{D}}_{l'_x}\left(\frac{\hat{\mathbf{D}}_{\varepsilon_y}}{\Delta t}-\frac{\hat{\mathbf{D}}_{\sigma_y}}{2}\right)\hat{\mathbf{E}}_y^{n} + \hat{\mathbf{D}}_{l_y}\hat{\mathbf{G}}_x^T\hat{\mathbf{H}}_z^{n+\frac{1}{2}} + \begin{bmatrix}\hat{\mathbf{D}}_{l_y}\hat{\mathbf{B}}_W & \hat{\mathbf{D}}_{l_y}\hat{\mathbf{B}}_E\end{bmatrix}\begin{bmatrix}\hat{\mathbf{H}}_W^{n+\frac{1}{2}}\\ \hat{\mathbf{H}}_E^{n+\frac{1}{2}}\end{bmatrix}, \quad (6)$$

where:

- $\hat{\mathbf{E}}_x$ and $\hat{\mathbf{E}}_y$ are column vectors collecting all E_x and E_y samples in the fine region, respectively;
- $\hat{\mathbf{D}}_{l_x}$, $\hat{\mathbf{D}}_{l_y}$ are diagonal matrices containing the length $\Delta\hat{x}$ and $\Delta\hat{y}$ of the primary edges along x and y, respectively;
- $\hat{\mathbf{D}}_{l'_x}$ and $\hat{\mathbf{D}}_{l'_y}$ are diagonal matrices. Their diagonal contains the length of the x-directed and y-directed edges of the secondary grid, respectively. The half-edges of length $\Delta\hat{x}/2$ and $\Delta\hat{y}/2$ that intersect the four boundaries are included;
- $\hat{\mathbf{D}}_{\varepsilon_x}$ and $\hat{\mathbf{D}}_{\varepsilon_y}$ are diagonal matrices containing the average permittivity on the x- and y-directed edges, respectively. Similarly, $\hat{\mathbf{D}}_{\sigma_x}$ and $\hat{\mathbf{D}}_{\sigma_y}$ contain the average conductivity on the same edges;
- Matrices $\hat{\mathbf{G}}_x$ and $\hat{\mathbf{G}}_y$ are the discrete derivative operators along x and y, respectively [17].
- $\hat{\mathbf{B}}_S$, $\hat{\mathbf{B}}_N$, $\hat{\mathbf{B}}_W$ and $\hat{\mathbf{B}}_E$ are the coefficient matrices that map the boundary fields to the appropriate equations, and are defined in [17].

2) Update Equation for the H_z Nodes: Since all magnetic nodes fall strictly inside the fine region, we can use a standard FDTD update for all of them [2]

$$\Delta\hat{x}\Delta\hat{y}\frac{\mu}{\Delta t}H_z\big|_{i+\frac{1}{2},j+\frac{1}{2}}^{n+\frac{1}{2}} = \Delta\hat{x}\Delta\hat{y}\frac{\mu}{\Delta t}H_z\big|_{i+\frac{1}{2},j+\frac{1}{2}}^{n-\frac{1}{2}} - \Delta\hat{x}E_x\big|_{i+\frac{1}{2},j}^{n} + \Delta\hat{x}E_x\big|_{i+\frac{1}{2},j+1}^{n} + \Delta\hat{y}E_y\big|_{i,j+\frac{1}{2}}^{n} - \Delta\hat{y}E_y\big|_{i+1,j+\frac{1}{2}}^{n}, \quad (7)$$

where μ denotes the average permittivity on the edge where $H_z\big|_{i+\frac{1}{2},j+\frac{1}{2}}^{n+\frac{1}{2}}$ is sampled. The set of equations (7) can be cast into matrix form

$$\hat{\mathbf{D}}_A\frac{\hat{\mathbf{D}}_\mu}{\Delta t}\hat{\mathbf{H}}_z^{n+\frac{1}{2}} = \hat{\mathbf{D}}_A\frac{\hat{\mathbf{D}}_\mu}{\Delta t}\hat{\mathbf{H}}_z^{n-\frac{1}{2}} + \hat{\mathbf{G}}_y\hat{\mathbf{D}}_{l_x}\hat{\mathbf{E}}_x^n - \hat{\mathbf{G}}_x\hat{\mathbf{D}}_{l_y}\hat{\mathbf{E}}_y^n, \quad (8)$$

where matrix $\hat{\mathbf{D}}_A$ is diagonal and contains the area of all primary cells. The diagonal matrix $\hat{\mathbf{D}}_\mu$ is instead formed by the average permittivity on each edge of the secondary grid [17].

B. Dynamical System Formulation

Update equations (5), (6) and (8) can be cast into the form of a discrete-time dynamical system

$$(\hat{\mathbf{R}}+\hat{\mathbf{F}})\hat{\mathbf{x}}^{n+1} = (\hat{\mathbf{R}}-\hat{\mathbf{F}})\hat{\mathbf{x}}^{n} + \hat{\mathbf{B}}\hat{\mathbf{u}}^{n+\frac{1}{2}}, \quad (9a)$$

$$\hat{\mathbf{y}}^{n} = \hat{\mathbf{L}}^T\hat{\mathbf{x}}^{n}. \quad (9b)$$

The state vector $\hat{\mathbf{x}}^n$ consists of all samples of E_x, E_y and H_z in the fine region, except for the hanging variables

$$\hat{\mathbf{x}}^n = \begin{bmatrix}\hat{\mathbf{E}}_x^n\\ \hat{\mathbf{E}}_y^n\\ \hat{\mathbf{H}}_z^{n-\frac{1}{2}}\end{bmatrix}. \quad (10)$$

The input $\hat{\mathbf{u}}^{n+\frac{1}{2}}$ and output $\hat{\mathbf{y}}^n$ of (9a)-(9b) contain all magnetic and electric fields on the North, South, West and East boundaries of the fine region

$$\hat{\mathbf{u}}^{n+\frac{1}{2}} = \begin{bmatrix}\hat{\mathbf{H}}_S^{n+\frac{1}{2}}\\ \hat{\mathbf{H}}_N^{n+\frac{1}{2}}\\ \hat{\mathbf{H}}_W^{n+\frac{1}{2}}\\ \hat{\mathbf{H}}_E^{n+\frac{1}{2}}\end{bmatrix}, \quad \hat{\mathbf{y}}^n = \begin{bmatrix}\hat{\mathbf{E}}_S^n\\ \hat{\mathbf{E}}_N^n\\ \hat{\mathbf{E}}_W^n\\ \hat{\mathbf{E}}_E^n\end{bmatrix}. \quad (11)$$

We can see that hanging variables are interpreted as the input of the FDTD model for the region, and the co-located electric fields are seen as the output. This input-output interpretation of the fine region equations is needed to apply MOR and, more importantly, to be able to reconnect the reduced model to the coarse grid without losing stability. Finally, the coefficients matrices in (9a)-(9b) can be written as [17]

$$\hat{\mathbf{R}} = \begin{bmatrix}\hat{\mathbf{R}}_{11}/\Delta t & -\frac{1}{2}\hat{\mathbf{K}}\\ -\frac{1}{2}\hat{\mathbf{K}}^T & \hat{\mathbf{R}}_{22}/\Delta t\end{bmatrix}, \quad (12)$$

$$\hat{\mathbf{F}} = \begin{bmatrix}\hat{\mathbf{F}}_{11} & -\frac{1}{2}\hat{\mathbf{K}}\\ \frac{1}{2}\hat{\mathbf{K}}^T & \mathbf{0}\end{bmatrix}, \quad (13)$$

$$\hat{\mathbf{B}} = \begin{bmatrix}\hat{\mathbf{D}}_{l_x}\hat{\mathbf{B}}_S & \hat{\mathbf{D}}_{l_x}\hat{\mathbf{B}}_N & \mathbf{0} & \mathbf{0}\\ \mathbf{0} & \mathbf{0} & \hat{\mathbf{D}}_{l_y}\hat{\mathbf{B}}_W & \hat{\mathbf{D}}_{l_y}\hat{\mathbf{B}}_E\\ \mathbf{0} & \mathbf{0} & \mathbf{0} & \mathbf{0}\end{bmatrix}, \quad (14)$$

$$\hat{\mathbf{L}} = \begin{bmatrix}-\hat{\mathbf{B}}_S & \hat{\mathbf{B}}_N & \mathbf{0} & \mathbf{0}\\ \mathbf{0} & \mathbf{0} & \hat{\mathbf{B}}_W & -\hat{\mathbf{B}}_E\\ \mathbf{0} & \mathbf{0} & \mathbf{0} & \mathbf{0}\end{bmatrix}, \quad (15)$$

where

$$\hat{\mathbf{R}}_{11} = \begin{bmatrix}\hat{\mathbf{D}}_{l_x}\hat{\mathbf{D}}_{l'_y}\hat{\mathbf{D}}_{\varepsilon_x} & \mathbf{0}\\ \mathbf{0} & \hat{\mathbf{D}}_{l_y}\hat{\mathbf{D}}_{l'_x}\hat{\mathbf{D}}_{\varepsilon_y}\end{bmatrix}, \quad \hat{\mathbf{R}}_{22} = \hat{\mathbf{D}}_A\hat{\mathbf{D}}_\mu, \quad (16)$$

$$\hat{\mathbf{F}}_{11} = \begin{bmatrix}\hat{\mathbf{D}}_{l_x}\hat{\mathbf{D}}_{l'_y}\frac{\hat{\mathbf{D}}_{\sigma_x}}{2} & \mathbf{0}\\ \mathbf{0} & \hat{\mathbf{D}}_{l_y}\hat{\mathbf{D}}_{l'_x}\frac{\hat{\mathbf{D}}_{\sigma_y}}{2}\end{bmatrix}, \quad (17)$$

$$\hat{\mathbf{K}} = \begin{bmatrix}-\hat{\mathbf{D}}_{l_x}\hat{\mathbf{G}}_y^T\\ \hat{\mathbf{D}}_{l_y}\hat{\mathbf{G}}_x^T\end{bmatrix}. \quad (18)$$

III. Structure-Preserving Model Order Reduction

Because of the grid refinement, the size of $\hat{\mathbf{x}}^n$ can be quite large, and significantly increase CPU time. To mitigate this issue, system (9a)-(9b) can be compressed using MOR. Among the many MOR methods available, we choose SPRIM [19], since it will preserve the block structure of (9a)-(9b). Using the robust Arnoldi iteration, SPRIM creates a projection matrix

$$\mathbf{V} = \begin{bmatrix} \mathbf{V}_1 & \mathbf{0} \\ \mathbf{0} & \mathbf{V}_2 \end{bmatrix} \tag{19}$$

suitable to approximate the full state vector $\hat{\mathbf{x}}^n$ through a new state vector $\tilde{\mathbf{x}}^n$ of smaller size

$$\hat{\mathbf{x}}^n \approx \mathbf{V}\tilde{\mathbf{x}}^n \,. \tag{20}$$

Matrix $\mathbf{V}$ consists of two blocks $\mathbf{V}_1$ and $\mathbf{V}_2$. The number of rows of $\mathbf{V}_1$ is equal to the number of electric field samples in $\hat{\mathbf{E}}_x^n$ and $\hat{\mathbf{E}}_y^n$. The number of rows in $\mathbf{V}_2$ is equal to the size of $\hat{\mathbf{H}}_z^{n-\frac{1}{2}}$. By substituting (20) into (9a)-(9b), and multiplying the first equation by $\mathbf{V}^T$ on the left, we obtain the reduced model

$$(\tilde{\mathbf{R}} + \tilde{\mathbf{F}})\tilde{\mathbf{x}}^{n+1} = (\tilde{\mathbf{R}} - \tilde{\mathbf{F}})\tilde{\mathbf{x}}^n + \tilde{\mathbf{B}}\hat{\mathbf{u}}^{n+\frac{1}{2}} \,, \tag{21a}$$

$$\tilde{\mathbf{y}}^n = \tilde{\mathbf{L}}^T\tilde{\mathbf{x}}^n \,, \tag{21b}$$

where

$$\tilde{\mathbf{R}} = \begin{bmatrix} \tilde{\mathbf{R}}_{11}/\Delta t & -\frac{1}{2}\tilde{\mathbf{K}} \\ -\frac{1}{2}\tilde{\mathbf{K}}^T & \tilde{\mathbf{R}}_{22}/\Delta t \end{bmatrix} \,, \quad \tilde{\mathbf{F}} = \begin{bmatrix} \tilde{\mathbf{F}}_{11} & -\frac{1}{2}\tilde{\mathbf{K}} \\ \frac{1}{2}\tilde{\mathbf{K}}^T & \mathbf{0} \end{bmatrix} \,, \tag{22}$$

$$\tilde{\mathbf{B}} = \mathbf{V}^T\hat{\mathbf{B}} \,, \quad \tilde{\mathbf{L}} = \mathbf{V}^T\hat{\mathbf{L}} \,, \tag{23}$$

$$\tilde{\mathbf{R}}_{11} = \mathbf{V}_1^T\hat{\mathbf{R}}_{11}\mathbf{V}_1 \,, \tag{24}$$

$$\tilde{\mathbf{R}}_{22} = \mathbf{V}_2^T\hat{\mathbf{R}}_{22}\mathbf{V}_2 \,, \tag{25}$$

$$\tilde{\mathbf{F}}_{11} = \mathbf{V}_1^T\hat{\mathbf{F}}_{11}\mathbf{V}_1 \,, \tag{26}$$

$$\tilde{\mathbf{K}} = \mathbf{V}_1^T\hat{\mathbf{K}}\mathbf{V}_2 \,. \tag{27}$$

The size of reduced model (21a)-(21b) is typically much lower than the size of (9a)-(9b). The size and accuracy of the reduced model can be controlled through the choice of the number of columns in the projection matrix $\mathbf{V}$. Because of the block-diagonal structure of (19), reduced model (21a)-(21b) inherits the block structure of the original FDTD equations (9a)-(9b), although its blocks are much smaller. The preservation of the peculiar structure of the FDTD equations will enable the extension of the CFL limit of the proposed scheme.

IV. Incorporation of the Reduced Model into the Main Coarse Grid

The goal of this section is to couple the reduced model to the coarse grid, while maintaining stability. An improper connection between different domains is indeed a common source of instability. Since the fields on the reduced model boundaries are sampled at a fine resolution, different from the resolution of the coarse grid, a suitable interpolation rule will be introduced. For coupling the reduced model to the coarse grid, we generalize the approach of [17] to handle reduced models. To realize the coupling, we will combine three sets of equations: the update equations for the reduced model (21a)-(21b), the update equation for the coarse grid nodes at the interface with the reduced model, and an interpolation rule.

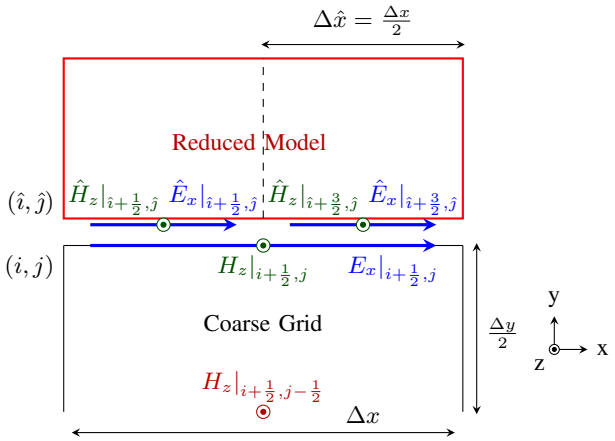

Fig. 2. Connection scenario considered in Sec. IV for the case of $r = 2$. A virtual gap has been inserted between the two subsystems for clarity.

A. State Equations for the Coarse Fields at the Interface

We consider the interface shown in Fig. 2 between the North boundary of the coarse grid, and the South boundary of the reduced model. The other edges can be treated similarly. For the E_x nodes of the coarse grid that fall at the interface with the reduced model, we introduce a hanging variable to facilitate the connection of the reduced model. The hanging variable is the magnetic field collocated with the electric field on the boundary. For example, in the case in Fig. 2, the hanging variable is $H_z|_{i+\frac{1}{2},j}$. Using this variable, a modified update equation analogous to (4) is written for $E_x|_{i+\frac{1}{2},j}$

$$\Delta x\frac{\Delta y}{2}\left(\frac{\varepsilon_x}{\Delta t} + \frac{\sigma_x}{2}\right)E_x|_{i+\frac{1}{2},j}^{n+1} = \Delta x\frac{\Delta y}{2}\left(\frac{\varepsilon_x}{\Delta t} - \frac{\sigma_x}{2}\right)E_x|_{i+\frac{1}{2},j}^{n} + \Delta x H_z|_{i+\frac{1}{2},j}^{n+\frac{1}{2}} - \Delta x H_z|_{i+\frac{1}{2},j-\frac{1}{2}}^{n+\frac{1}{2}} \,. \tag{28}$$

In (28), ε_x and σ_x are the permittivity and conductivity in the half coarse cell below the interface. The hanging variable $H_z|_{i+\frac{1}{2},j}^{n+\frac{1}{2}}$ can be considered as the input for the coarse grid. The use of the hanging variable $H_z|_{i+\frac{1}{2},j}^{n+\frac{1}{2}}$ is necessary since a standard FDTD equation for $E_x|_{i+\frac{1}{2},j}^{n+1}$ would involve a magnetic field sample inside the reduced model, which is not available. We will also see in the next section that, through hanging variables, we can systematically ensure stability.

For all edges at the boundary of the coarse grid, a hanging variable and an equation analogous to (28) is defined. All these update equations can be written in matrix form as

$$\mathbf{D}_l\mathbf{D}_{l'}\left(\frac{\mathbf{D}_\varepsilon}{\Delta t} + \frac{\mathbf{D}_\sigma}{2}\right)\mathbf{y}^{n+1} = \mathbf{D}_l\mathbf{D}_{l'}\left(\frac{\mathbf{D}_\varepsilon}{\Delta t} - \frac{\mathbf{D}_\sigma}{2}\right)\mathbf{y}^{n} + \mathbf{D}_l\mathbf{G}^T\mathbf{H}^{n+\frac{1}{2}} - \mathbf{D}_l\mathbf{G}^T\mathbf{U}^{n+\frac{1}{2}} \,, \tag{29}$$

where $\mathbf{y}^n$ collects all the coarsely-sampled electric fields at the interfaces, and $\mathbf{D}_\varepsilon$ and $\mathbf{D}_\sigma$ are the diagonal matrices

containing the permittivity and conductivity values in the half cells on the coarse grid boundary. Matrix $\mathbf{D}_l$ is diagonal and contains the length of the coarse grid on the interface. Diagonal matrix $\mathbf{D}_{l'}$ contains the length of the half edges of the coarse grid that intersect the interface. Matrix $\mathbf{G}$ is diagonal and contains only -1 and $+1$. Vector $\mathbf{H}^{n+\frac{1}{2}}$ contains the magnetic fields in the coarse grid near the interface with the reduced model. Input vector $\mathbf{U}^{n+\frac{1}{2}}$ collects all the hanging variables on the coarse side of the interface, such as $H_z|^{n+\frac{1}{2}}_{i+\frac{1}{2},j}$ in Fig. 2.

B. Interpolation Rule

The fields at the boundaries of the coarse mesh and of the reduced model need to be linked by a suitable interpolation rule. This is necessary to satisfy boundary conditions, and because they are sampled at different resolution. We use the interpolation rule in [17], which will ensure stability, as we shall see in the next section. Between the boundary electric fields, we impose the following relation

$$\tilde{\mathbf{y}}^n = \mathbf{T}\mathbf{y}^n \qquad \forall n\,, \tag{30}$$

where $\mathbf{T}$ is the transformation matrix that sets adjacent coarse and fine grid electric fields to be equal. As discussed in [17], a reciprocal constraint must be imposed on the magnetic fields on the boundary in order to ensure stability

$$\mathbf{U}^{n+\frac{1}{2}} = \frac{1}{r}\mathbf{T}^T\hat{\mathbf{u}}^{n+\frac{1}{2}} \qquad \forall n\,. \tag{31}$$

C. Coupling of Reduced Model and Coarse Grid

The final update equations for the reduced model are derived by combining the reduced model (21a)-(21b), update equation (29) for the boundary fields of the coarse grid, and interpolation rules (30) and (31). First, we substitute (31) into (29)

$$\mathbf{D}_l\mathbf{D}_{l'}\left(\frac{\mathbf{D}_\varepsilon}{\Delta t}+\frac{\mathbf{D}_\sigma}{2}\right)\mathbf{y}^{n+1} = \mathbf{D}_l\mathbf{D}_{l'}\left(\frac{\mathbf{D}_\varepsilon}{\Delta t}-\frac{\mathbf{D}_\sigma}{2}\right)\mathbf{y}^n + \mathbf{D}_l\mathbf{G}^T\mathbf{H}^{n+\frac{1}{2}} - \frac{1}{r}\mathbf{D}_l\mathbf{G}^T\mathbf{T}^T\hat{\mathbf{u}}^{n+\frac{1}{2}}\,. \tag{32}$$

Then, equation (30) is substituted into (21b)

$$\mathbf{T}\mathbf{y}^{n+1} = \tilde{\mathbf{L}}\tilde{\mathbf{x}}^{n+1}\,. \tag{33}$$

Equations (21a), (32), and (33) are combined in a linear system

$$\mathbf{A}_1\mathbf{z}^{n+1} = \mathbf{A}_2\mathbf{z}^n + \mathbf{D}_l\mathbf{G}^T\begin{bmatrix}\mathbf{H}^{n+\frac{1}{2}}\\ \mathbf{0}\\ \mathbf{0}\end{bmatrix}\,, \tag{34}$$

where

$$\mathbf{z}^n = \begin{bmatrix}\mathbf{y}^n\\ \hat{\mathbf{u}}^{n-\frac{1}{2}}\\ \tilde{\mathbf{x}}^n\end{bmatrix}\,, \tag{35}$$

$$\mathbf{A}_1 = \begin{bmatrix}\mathbf{D}_l\mathbf{D}_{l'}\left(\frac{\mathbf{D}_\varepsilon}{\Delta t}+\frac{\mathbf{D}_\sigma}{2}\right) & \frac{1}{r}\mathbf{D}_l\mathbf{G}^T\mathbf{T}^T & \mathbf{0}\\ \mathbf{T} & \mathbf{0} & -\tilde{\mathbf{L}}^T\\ \mathbf{0} & -\tilde{\mathbf{B}} & (\tilde{\mathbf{R}}+\tilde{\mathbf{F}})\end{bmatrix}\,, \tag{36}$$

$$\mathbf{A}_2 = \begin{bmatrix}\mathbf{D}_l\mathbf{D}_{l'}\left(\frac{\mathbf{D}_\varepsilon}{\Delta t}-\frac{\mathbf{D}_\sigma}{2}\right) & \mathbf{0} & \mathbf{0}\\ \mathbf{0} & \mathbf{0} & \mathbf{0}\\ \mathbf{0} & \mathbf{0} & (\tilde{\mathbf{R}}-\tilde{\mathbf{F}})\end{bmatrix}\,. \tag{37}$$

Multiplying (34) on the left by $\mathbf{A}_1^{-1}$, we obtain

$$\mathbf{z}^{n+1} = \mathbf{A}_1^{-1}\mathbf{A}_2\mathbf{z}^n + \mathbf{A}_1^{-1}\mathbf{D}_l\mathbf{G}^T\begin{bmatrix}\mathbf{H}^{n+\frac{1}{2}}\\ \mathbf{0}\\ \mathbf{0}\end{bmatrix}\,. \tag{38}$$

Equation (38) is explicit, and is used to update the state of the reduced model $\tilde{\mathbf{x}}^n$, and the electric fields $\mathbf{y}^n$ at the interface with the coarse grid. The coefficient matrices in (38) can be precomputed once before runtime. A sparse LU factorization can be performed on $\mathbf{A}_1$ to efficiently compute its inverse multiplied by $\mathbf{A}_2$ and $\mathbf{D}_l\mathbf{G}^T$. Ultimately, the proposed scheme consists of conventional FDTD equations to update the coarse grid, and (38) to update the reduced model state and the interface. If multiple reduced models are present, equation (38) is applied to each one of them.

V. Stability Analysis and CFL Limit Extension

In this section, we analyse the stability of the FDTD scheme with embedded reduced models. We derive the CFL limit of the proposed scheme, and show how it can be extended. We use the stability theory proposed in [17], which is based on the concept of energy dissipation. This theory is particularly convenient to investigate the stability of advanced FDTD setups where different meshes and models are coupled together.

A. Passivity of the Coarse Grid and the Interpolation Rule

From the perspective of system theory, the obtained scheme can be seen as the connection of three subsystems: the coarse mesh, the interpolation rule, and the reduced model. If all subsystems are passive, i.e. unable to generate energy on their own, the final scheme will be passive by construction, and thus stable [17], [20]. As proved in [17], the coarse mesh is passive for any time step satisfying its own CFL limit. Interpolation rule (30)-(31) can be shown to be lossless for any time step [17]. In order to establish the stability of the overall scheme, we have to investigate when the reduced model is passive.

B. Passivity Conditions for the Fine Grid

The reduced model has been derived from the fine grid model (9a)-(9b). In order to be passive, this model must satisfy the following three passivity conditions [17]

$$\hat{\mathbf{R}} = \hat{\mathbf{R}}^T > 0\,, \tag{39a}$$

$$\hat{\mathbf{F}} + \hat{\mathbf{F}}^T \geq 0\,, \tag{39b}$$

$$\hat{\mathbf{B}} = \hat{\mathbf{L}}\hat{\mathbf{S}}\,, \tag{39c}$$

where

$$\hat{\mathbf{S}} = \hat{\mathbf{L}}^T\hat{\mathbf{B}} = \begin{bmatrix}-\Delta\hat{x}\mathbf{I}_{\hat{N}_x} & \mathbf{0} & \mathbf{0} & \mathbf{0}\\ \mathbf{0} & \Delta\hat{x}\mathbf{I}_{\hat{N}_x} & \mathbf{0} & \mathbf{0}\\ \mathbf{0} & \mathbf{0} & \Delta\hat{y}\mathbf{I}_{\hat{N}_y} & \mathbf{0}\\ \mathbf{0} & \mathbf{0} & \mathbf{0} & -\Delta\hat{y}\mathbf{I}_{\hat{N}_y}\end{bmatrix}\,. \tag{40}$$

Condition (39a) can be shown to be a generalization of the CFL limit for a region with inhomogeneous materials [17]. Condition (39b) is satisfied if all conductivities σ_x and σ_y in the fine region are non-negative, which is usually the case. It can be shown, by direct substitution, that (39c) always holds. In conclusion, the original model for the fine grid (9a)-(9b) is passive under the CFL limit of the fine grid [17].

C. Passivity of the Reduced Model

We now investigate the passivity of the reduced model (21a)-(21b) that has been produced for the fine grid. The reduced model will be passive if [17]

$$\tilde{\mathbf{R}} = \tilde{\mathbf{R}}^T > 0\,, \tag{41a}$$

$$\tilde{\mathbf{F}} + \tilde{\mathbf{F}}^T \geq 0\,, \tag{41b}$$

$$\tilde{\mathbf{B}} = \tilde{\mathbf{L}}\hat{\mathbf{S}}\,. \tag{41c}$$

The following theorem shows that, by construction, the proposed reduction process preserves the passivity of the fine grid model, which is a novel result.

Theorem 1. *Reduced model* (21a)-(21b) *is passive for any* Δt *that satisfies the CFL limit* (39a) *of the fine grid.*

Proof. Since $\mathbf{V}$ is full rank by construction, and $\tilde{\mathbf{R}} = \mathbf{V}^T\hat{\mathbf{R}}\mathbf{V}$, condition (39a) implies (41a). In the same way, since $\tilde{\mathbf{F}} = \mathbf{V}^T\hat{\mathbf{F}}\mathbf{V}$, condition (39b) implies (41b). Finally, by multiplying (39c) on the left by $\mathbf{V}^T$, we obtain (41c). □

D. Stability of the FDTD Scheme with Reduced Models

To summarize, we have shown that:

- the interpolation rule is lossless, and thus passive, for any Δt;
- the coarse grid is passive for any Δt under its own CFL limit;
- the reduced model of the fine grid is passive for any Δt under the CFL limit of the fine grid.

The overall scheme, which results from the connection of these three subsystems, will be passive and stable under the most restrictive CFL limit, which is the one of the fine grid. For larger time steps, the reduced model becomes active, and destabilizes the whole scheme. We have provided a formal proof of stability of the proposed FDTD scheme with reduced models. The proof can be trivially extended to the case of multiple reduced models, where one must simply require all reduced models to be passive. The ability to handle an arbitrary number of reduced models is a significant advantage previous results [16].

E. Extension of the CFL Limit

As discussed in the previous section, the overall stability limit is dictated by the most restrictive CFL limit of the embedded models. This constrain can be relaxed by extending the CFL limit of the reduced models prior to their connection to the main grid. The extension can be achieved with a simple perturbation of the model coefficients. For a time step beyond the CFL limit of a given reduced model, conditions (41b) and (41c) will still hold, since they are independent from Δt. Condition (41a) will be violated, but can be restored with a perturbation of $\tilde{\mathbf{K}}$. We use the method proposed in [21]. Using the Schur's compliment [22], one can show that (41a) is equivalent to

$$s_k \leq \frac{2}{\Delta t} \quad \forall k\,. \tag{42}$$

where s_k are the singular values of $\tilde{\mathbf{R}}_{11}^{-\frac{1}{2}}\tilde{\mathbf{K}}\tilde{\mathbf{R}}_{22}^{-\frac{1}{2}}$. Above the CFL limit of the reduced model, some singular values will exceed the threshold in (42). By perturbing $\tilde{\mathbf{K}}$ with the method in [21], condition (42) can be enforced. This enforcement enables the use of a larger time step in the *whole* domain, including the entire coarse grid, and results in a significant saving of CPU time. Numerical tests in Sec. VI will show that an extension of the CFL limit by 2X or 3X can be typically achieved with minimal impact on accuracy. A remarkable aspect is that we can enhance the stability limit of the entire scheme by acting only on the reduced model. This is a main novelty compared to [21], where MOR and singular value perturbation had to be applied to the equations of the whole system. This feature makes the proposed method more efficient and scalable.

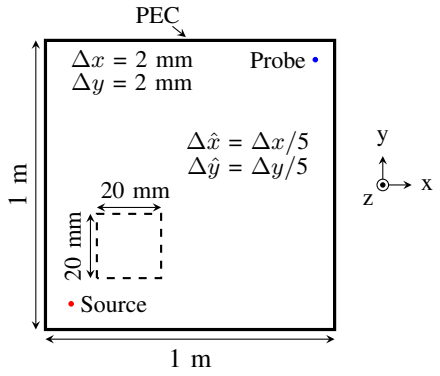

Fig. 3. Layout of the PEC cavity considered in Sec. VI-A. The dashed box denotes the refinement region.

VI. Numerical Examples

Several test cases are provided to numerically validate the stability and performance of the proposed method, which was implemented in Matlab with vectorized operations for maximum efficiency. Simulations were run on a computer with a 3.6 GHz CPU and 8 GB of memory.

A. 2D Cavity

In this section, the proposed method is applied to the empty 1 m × 1 m 2D cavity in Fig. 3. The cavity has perfect electric conductor (PEC) walls. The whole region is discretized with a coarse mesh with Δx = Δy = 2 mm, except for a central 0.2 m × 0.2 m area, discretized with a fine mesh ($r = 5$). The purpose of this test is to verify the stability of the proposed method. The cavity is excited by a Gaussian pulse source with bandwidth of 0.5 GHz.

Using the proposed technique, a reduced model was created from the FDTD equations of the fine region (9a)-(9b). MOR

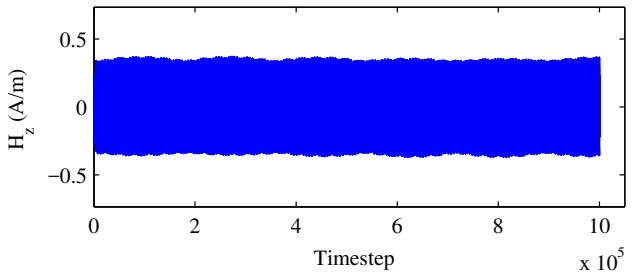

Fig. 4. Magnetic field at the probe for the the empty cavity of Sec. VI-A, computed with the proposed method for 10^6 time steps.

Table I
EXECUTION TIME FOR THE 2D CAVITY IN SEC.VI-A. THE MOR TIME IS INCLUDED IN THE RUNTIME. THE CFL NUMBER IS DEFINED AS THE RATIO OF THE TIME STEP Δt USED IN THE SIMULATION AND THE CFL LIMIT.

Method	CFL number	Runtime	Speed-up
FDTD, all-coarse grid	0.99	9.0 s	-
FDTD, all-fine grid	0.99	451.2 s	-
Subgridding	0.99	95.3 s	4.7X
Proposed (MOR only)	0.99	131.1 s	3.4X
Proposed (CFL extension only)	1.98	340.1 s	1.3X
Proposed	1.98	58.6 s	7.7X

reduced their order from 7,600 to 1,200. The CFL limit of the reduced model was extended by 2X, prior to its embedding into the coarse mesh. The proposed method was run for 10^6 time steps. The computed magnetic field at the probe, shown in Fig. 4, confirms the stability of the proposed method.

Table I gives the CPU time taken by the proposed method, by standard FDTD with an all-coarse mesh, by standard FDTD with an all-fine mesh, and by a subgridding method [17]. The proposed method was also tested with MOR enabled but no CFL limit extension, and vice versa. All methods were run with a time step at 99% of their CFL limit which, for the methods with CFL limit extension, corresponds to 1.98% of the original CFL limit. In terms of accuracy, all methods are in very good agreement, as shown in Fig. 5. Since, in this case, the fine region does not contain any complex object, all methods are expected to give comparable accuracy. In terms of execution time, the proposed method provides a 7.7X speed-up with respect to a complete refinement of the FDTD mesh, and a 60% gain versus subgridding. We can see that both MOR and the extension of the CFL limit of the reduced model contribute to the computational gains of the proposed method.

B. Waveguide with Irises

We consider the 4 m $\times$ 0.7 m waveguide shown in Fig. 6. The waveguide includes two thin PEC irises [13]. A coarse mesh is used in most of the domain, with resolution $\Delta x = \Delta y = 0.05\,\mathrm{m}$. The two areas around the irises were instead meshed with a refined grid ($r = 3$) in order to capture the irregular fields caused by the discontinuity. The refined regions are 0.5 m $\times$ 0.5 m wide, and are shown in Fig. 6. In the proposed method, two reduced models were generated for these regions and embedded into the coarse grid. The ends of the waveguide are terminated with perfectly matched layer which is 10 coarse cells deep. The waveguide is excited by a

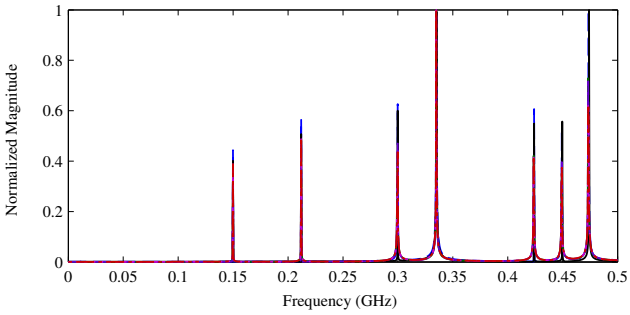

Fig. 5. Frequency response of the cavity of Sec. VI-A, obtained with FDTD with an all-coarse mesh (– — –), FDTD with an all-fine mesh (——), subgridding (——), the proposed method with only MOR (— —), the proposed method with only CFL extension (- - - -), and the proposed method with both MOR and CFL extension (- — -).

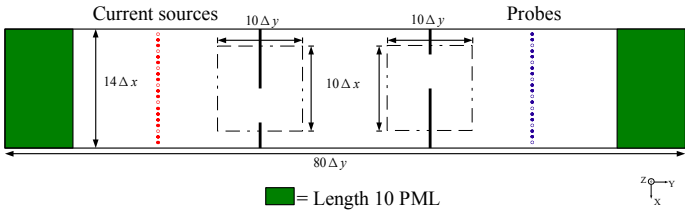

Fig. 6. Geometry of the waveguide with irises considered in Sec. VI-B. The boxes indicate the regions replaced by a reduced model.

Gaussian pulse with 0.4 GHz bandwidth. A probe is located at the other end. All methods were run at 0.99 times their CFL limit. In the proposed method, the CFL limit was extended by two times, and MOR reduced the size of each fine grid models from 2,760 to 648.

Fig. 7 compares the frequency response obtained with FDTD, subgridding [17] and the proposed method. We can clearly see that a coarse mesh does not accurately capture the frequency response of the system, due to its inability to properly resolve the irregular fields around the apertures. The other methods, which utilize a fine grid in the two critical regions, are in very good agreement with an all-fine FDTD simulation. In terms of runtime, Table II shows that subgridding is only marginally faster than an all-fine simulation, and that the proposed method provides the highest speed up among the compared techniques. For this case, the speed-up is more modest than in the previous example, due to the presence of two refined regions and their size relative to the overall problem.

C. Reflection Test

To further investigate the accuracy of the proposed scheme, we analyse the reflections from a scatterer placed in a waveguide. A 66 mm $\times$ 40 mm structure terminated with 15 mm-thick perfectly matched layers on two sides is considered. The layout of the structure is shown in Fig. 8. The scatterer is comprised of four small copper rods with 1 mm radius. A line source is used to excite the waveguide and a line probe near the source position is chosen. The structure is uniformly discretized with coarse cells with $\Delta x = \Delta y = 1\,\mathrm{mm}$. In the proposed method, the region where the four rods are located

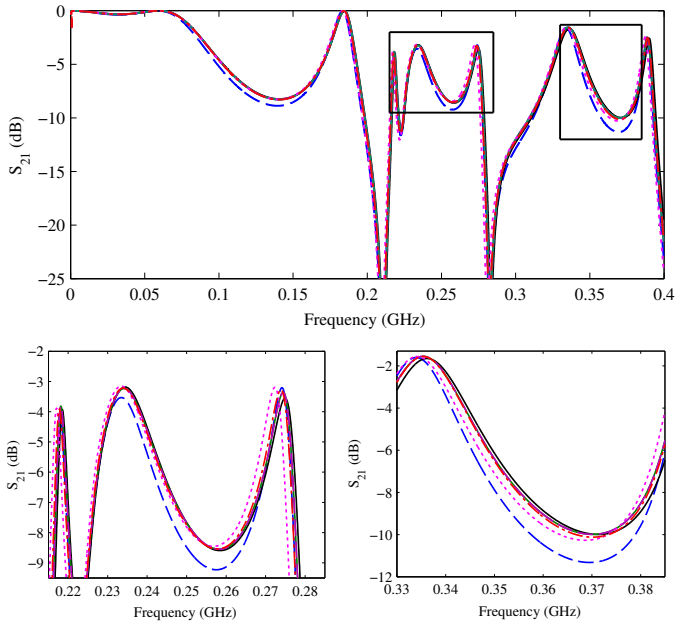

Fig. 7. Frequency response of the waveguide of Sec. VI-B, obtained with FDTD with an all-coarse mesh (– – –), FDTD with an all-fine mesh (——), subgridding (——), proposed method with only MOR (— —), proposed method with only CFL extension (- - - -), and proposed method with both MOR and CFL limit extension (- — -).

Table II
EXECUTION TIME FOR THE WAVEGUIDE STRUCTURE IN SEC. VI-B.

Method	CFL number	Runtime	Speed-up
FDTD, all-coarse grid	0.99	28.9 s	-
FDTD, all-fine grid	0.99	281.2 s	-
Subgridding	0.99	222.0 s	1.26X
Proposed (MOR only)	0.99	245.4 s	1.15X
Proposed (CFL extension only)	1.98	484.3 s	0.58X
Proposed	1.98	118.5 s	2.37X

is refined with $r = 6$. All methods were run with a time step equal to 0.99 times their CFL limit. In the proposed method, MOR was used to reduce the number of variables in the fine region from 7,008 to 1,920. The CFL limit of the reduced model was extended by 3 times without incurring in a significant reduction of accuracy.

The reflected power measured with all methods is shown in the top panel of Fig. 9. A conventional FDTD run with a coarse grid everywhere overestimates the reflections from the rods across the entire frequency range, confirming the need for a finer mesh around the scatterers. The proposed method and subgridding are instead in very good agreement with the reference simulation, which was performed with FDTD and a fine mesh in the entire computational domain. In terms of performance, the proposed method is 27.5 times faster than an all-fine FDTD simulation, and 2.1 times faster than subgridding, as reported in Table III. In order to further assess the accuracy of the proposed method, we finally repeated the analysis of the waveguide without the four rods. The purpose of this test is to measure the level of reflections caused by the transition from the coarse grid to the reduced model of the fine grid. The reflections from the interface obtained with

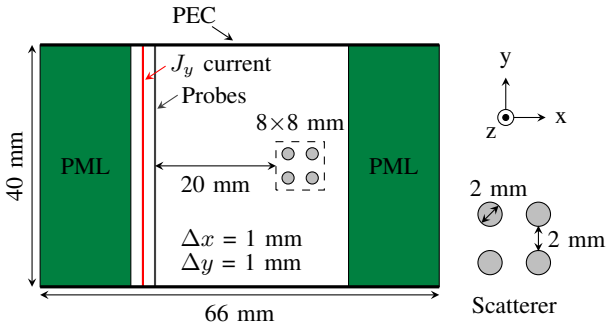

Fig. 8. Layout of the four-rod reflection test in Sec. VI-C. The dashed line shows the area modeled with a fine grid, and replaced by a reduced model in the proposed technique.

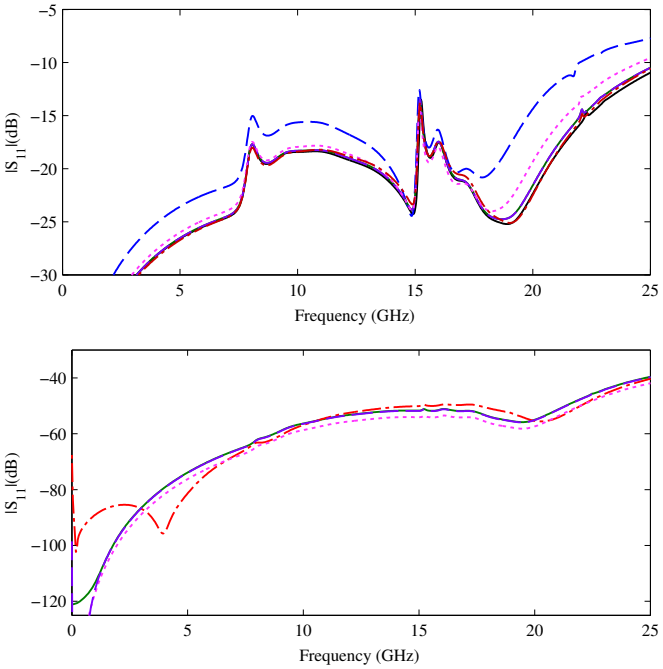

Fig. 9. Reflected power with respect to the incident for the test in Sec. VI-C. Top panel: reflections from the four-rod scatterer. Bottom panel: reflections with no rods inside. Results were computed with an FDTD with an all-coarse mesh (– – –), an all-fine mesh (——), subgridding (——), the proposed method with only MOR (— —), the proposed method with only CFL extension (- - - -), and the proposed method with both MOR and CFL limit extension (- — -).

both subgridding and the proposed method are depicted in the bottom panel of Fig. 9. The figure shows that the proposed method can provide, for a given region, a reduced model with enhanced CFL limit that can be seamlessly embedded into an FDTD grid, without resulting in increased reflections or stability issues.

VII. CONCLUSION

In this paper, we proposed a stable FDTD scheme which supports the inclusion of reduced models to capture complex objects with fine features. Initially, complex objects are discretized with a refined mesh, in order to properly capture their geometry. Then, the FDTD equations for each refined region are compressed with model order reduction. The reduced

Table III
EXECUTION TIME FOR THE FOUR RODS SCATTERING TEST IN SEC. VI-C.

Method	CFL number	Runtime	Speed-up
FDTD, all-coarse grid	0.99	4.0 s	-
FDTD, all-fine grid	0.99	654.2 s	-
Subgridding	0.99	50.5 s	12.9X
Proposed (MOR only)	0.99	68.4 s	9.6X
Proposed (CFL extension only)	2.97	537.2 s	1.2X
Proposed	2.97	23.8 s	27.5X

models are finally coupled to the surrounding coarse mesh. The proposed method supports the embedding of multiple reduced models, losses and inhomogeneous material properties. The stability and CFL limit of the resulting scheme can be rigorously proved, which is a novel result. The CFL limit can be also extended, with negligible accuracy loss, with a simple perturbation of the model coefficients. Numerical tests confirm the stability of the proposed method, and its potential to increase FDTD's efficiency for multiscale problems. Future works will extend the proposed ideas to the three-dimensional case.

REFERENCES

[1] K. Yee, "Numerical solution of initial boundary value problems involving Maxwell's equations in isotropic media," *IEEE Trans. Antennas Propag.*, vol. 14, no. 3, pp. 302–307, 1966.

[2] S. D. Gedney, *Introduction to the Finite-Difference Time-Domain (FDTD) Method for Electromagnetics*, 1st ed. San Rafael, CA: Morgan & Claypool Publishers, 2011.

[3] J. Boonzaaler and C. Pistorius, "Radiation and scattering by thin wires with a dielectric coatinga finite-difference time-domain approach," *Microw. Opt. Technol. Lett.*, vol. 5, no. 6, pp. 288–291, 1992.

[4] J.-P. Berenger, "A multiwire formalism for the FDTD method," *IEEE Trans. Electromagn. Compat.*, vol. 42, no. 3, pp. 257–264, 2000.

[5] J. G. Maloney and G. S. Smith, "The efficient modeling of thin material sheets in the finite-difference time-domain (FDTD) method," *IEEE Trans. Antennas Propag.*, vol. 40, no. 3, pp. 323–330, 1992.

[6] K.-P. Ma, M. Li, J. L. Drewniak, T. H. Hubing, and T. P. Van Doren, "Comparison of FDTD algorithms for subcellular modeling of slots in shielding enclosures," *IEEE Trans. Electromagn. Compat.*, vol. 39, no. 2, pp. 147–155, 1997.

[7] P. Thoma and T. Weiland, "A consistent subgridding scheme for the finite difference time domain method," *Int. J. Numer. Model El.*, vol. 9, no. 5, pp. 359–374, 1996.

[8] K. Xiao, D. J. Pommerenke, and J. L. Drewniak, "A three-dimensional FDTD subgridding algorithm with separated temporal and spatial interfaces and related stability analysis," *IEEE Trans. Antennas Propag.*, vol. 55, no. 7, pp. 1981–1990, 2007.

[9] Y. Wang, S. Langdon, and C. Penney, "Analysis of accuracy and stability of FDTD subgridding schemes," in *2010 European Microwave Conf.*, 2010, pp. 1297–1300.

[10] A. C. Cangellaris and L. Zhao, "Rapid FDTD simulation without time stepping," *IEEE Microw. Guided Wave Lett.*, vol. 9, no. 1, pp. 4–6, 1999.

[11] B. Denecker, F. Olyslager, L. Knockaert, and D. De Zutter, "Generation of FDTD subcell equations by means of reduced order modeling," *IEEE Trans. Antennas Propag.*, vol. 51, no. 8, pp. 1806–1817, 2003.

[12] L. Kulas and M. Mrozowski, "Reduced order models of refined Yee's cells," *IEEE Microw. Wireless Compon. Lett.*, vol. 13, no. 4, pp. 164–166, 2003.

[13] X. Li and P. Triverio, "Stable FDTD Simulations with Subgridding at the Time Step of the Coarse Grid: a Model Order Reduction Approach," in *IEEE MTT-S Int. Conf. on Numerical Electromagnetic and Multiphysics Modeling and Optimization*, Ottawa, Canada, August 11–14 2015.

[14] C. Chang and C. D. Sarris, "A Spatially Filtered Finite-Difference Time-Domain Scheme With Controllable Stability Beyond the CFL Limit: Theory and Applications," *IEEE Trans. Microw. Theory Techn.*, vol. 61, no. 1, pp. 351–359, Jan 2013.

[15] M. Gaffar and D. Jiao, "An explicit and unconditionally stable FDTD method for 3-D electromagnetic analysis," in *2013 IEEE MTT-S Int. Microwave Symp. Dig.*, June 2013.

[16] L. Kulas and M. Mrozowski, "Stability of the FDTD scheme containing macromodels," *IEEE Microw. Wireless Compon. Lett.*, vol. 14, no. 10, pp. 484–486, 2004.

[17] F. Bekmambetova, X. Zhang, and P. Triverio, "A Dissipative Systems Theory for FDTD with Application to Stability Analysis and Subgridding ," *IEEE Trans. Antennas Propag.*, 2016, (submitted).

[18] N. V. Venkatarayalu, R. Lee, Y.-B. Gan, and L.-W. Li, "A stable FDTD subgridding method based on finite element formulation with hanging variables," *IEEE Trans. Antennas Propag.*, vol. 55, no. 3, pp. 907–915, 2007.

[19] R. W. Freund, "SPRIM: Structure-preserving reduced-order interconnect macromodeling," in *Proceedings of the 2004 IEEE/ACM International Conference on Computer-aided Design*, ser. ICCAD '04. Washington, DC, USA: IEEE Computer Society, 2004, pp. 80–87.

[20] P. Triverio, S. Grivet-Talocia, M. S. Nakhla, F. Canavero, R. Achar, "Stability, causality, and passivity in electrical interconnect models," *IEEE Trans. Adv. Packag.*, vol. 30, no. 4, pp. 795–808, 2007.

[21] X. Li, C. D. Sarris, and P. Triverio, "Structure-Preserving Reduction of Finite-Difference Time-Domain Equations with Controllable Stability Beyond the CFL Limit," *IEEE Trans. Microw. Theory Techn.*, vol. 62, no. 12, pp. 3228–3238, 2014.

[22] G. H. Golub and C. F. V. Loan, *Matrix Computations*. Johns Hopkins University Press, 1996.